# Femtosecond Field-Driven On-Chip Unidirectional Electronic Currents in Nonadiabatic Tunneling Regime

*Liping Shi, Ihar Babushkin,* Anton Husakou, Oliver Melchert, Bettina Frank, Juemin Yi, Gustav Wetzel, Ayhan Demircan, Christoph Lienau, Harald Giessen, Misha Ivanov, Uwe Morgner, and Milutin Kovacev*

**Recently, asymmetric plasmonic nanojunctions have shown promise as on-chip electronic devices to convert femtosecond optical pulses to current bursts, with a bandwidth of multi-terahertz scale, although yet at low temperatures and pressures. Such nanoscale devices are of great interest for novel ultrafast electronics and opto-electronic applications. Here, the device is operated in air and at room temperature, revealing the mechanisms of photoemission from plasmonic nanojunctions, and the fundamental limitations on the speed of optical-to-electronic conversion. Inter-cycle interference of coherent electronic wavepackets results in a complex energy electron distribution and birth of multiphoton effects. This energy structure, as well as reshaping of the wavepackets during their propagation from one tip to the other, determine the ultrafast dynamics of the current. It is shown that, up to some level of approximation, the electron flight time is well-determined by the mean ponderomotive velocity in the driving field.**

## 1. Introduction

As known from atomic physics,[1–4] with increase of the incident laser intensity, the ionization dynamics undergoes a transition from a relatively slow multiphoton process to fast sub-cycle bursts, referred to as tunneling ionization. The dimensionless Keldysh parameter $\gamma = 2\pi\tau_{\mathrm{T}}/T$ characterizes, relative to the optical cycle duration $T$, a typical time $\tau_{\mathrm{T}} = \sqrt{2m\phi}/|eE|$, required for an electron to nearly completely leave the atom with the ionization potential $\phi$ in an external field of the amplitude $E$ (here $m$ and $e$ are the electron mass and charge). In the multiphoton regime ($\gamma \gg 1$), electrons require many optical cycles to be ionized. It is easier to describe such a process in the frequency-domain as an absorption of $n = \phi/\hbar\omega$ photons of energy $\hbar\omega$. But in the tunneling regime ($\gamma \ll 1$) electrons escape from the nucleus during a small fraction of an optical cycle, and thus the description in the time-domain is more convenient. Nevertheless, time- and frequency-domain descriptions represent the same process. In particular, multiphoton dynamics can be also described in time-domain, as an interference among the electronic wavepackets[3,5]

L. Shi
Key Laboratory of 3D Micro/Nano Fabrication and Characterization of Zhejiang Province
School of Engineering
Westlake University
18 Shilongshan Road, Hangzhou 310024, China

L. Shi
Institute of Advanced Technology
Westlake Institute for Advanced Study
18 Shilongshan Road, Hangzhou 310024, China

I. Babushkin, O. Melchert, A. Demircan, U. Morgner, M. Kovacev
Institute of Quantum Optics
Leibniz University Hannover
Welfengarten 1, Hannover 30167, Germany
E-mail: babushkin@iqo.uni-hannover.de

I. Babushkin, O. Melchert, A. Demircan, U. Morgner, M. Kovacev
Cluster of Excellence PhoenixD (Photonics, Optics, and Engineering-Innovation Across Disciplines)
Hannover 30167, Germany

I. Babushkin, A. Husakou, M. Ivanov
Max Born Institute
Max-Born-Str. 2a, Berlin 12489, Germany

B. Frank, H. Giessen
Universität Stuttgart
Pfaffenwaldring 57, Stuttgart 70569, Germany

J. Yi, C. Lienau
Institute of Physics and Center of Interface Science
Carl von Ossietzky University Oldenburg
Oldenburg 26129, Germany

G. Wetzel
Institute of Electronic Materials and Devices
Leibniz University Hannover
Schneiderberg 32, Hannover 30167, Germany

The ORCID identification number(s) for the author(s) of this article can be found under https://doi.org/10.1002/lpor.202000475



**DOI: 10.1002/lpor.202000475**

created at different optical cycles. This fact was utilized in the Yudin–Ivanov (Y–I) model,[6] where both multiphoton and tunneling regimes were described in a single formula. In this unified description, the time-domain tunneling picture is used. Yet, the electron ionization dynamics differ in these two regimes, demonstrating sub-cycle features in the tunneling regime and much slower dynamics in the multiphoton one. In the intermediate regime, $\gamma \approx 1$, both fast and slow components appear.

This tunneling picture arose from atomic physics, and has also been proven valid for photoemission at surfaces of metallic nanotips.[7–12] Although the electronic wavefunctions inside the metal are not localized, an approximation of localized wavefunctions still yields good results when considering ionization from metallic surfaces.[8,9,11,12] Strong near-field enhancement near the nanotips triggers electrons near the Fermi level to tunnel through the surface on a sub-cycle timescale,[7,8,12–21] which is of particular interest in ultrafast time-resolved electron nanoscopy.[12,21–25] Interference of the wavepackets tunneled at different cycles gives rise to pronounced peaks in the electron spectra separated by the energy of the pump photons.[8,11,12,21]

Recently, ultrafast electron emission from gold dimer nanoantennas (nanojunctions) with gap sizes down to the few nanometer scale has attracted great interest for on-chip petahertz electronics.[25–27] When embedding such a nanojunction into a closed circuit, unidirectional electronic optically controllable currents bursts, which vary on the sub-cycle scale, may arise,[26,27] if few-cycle driving pulses with controlled carrier-envelope phase (CEP) are used. Especially interesting in this respect is the recent proposal to create ultrafast unidirectional currents in asymmetric nanostructures,[28] which enables a DC bias without necessity of CEP control of the driving pulse.

Since gold nanoantennas cannot withstand strong electric fields due to the limitations of photothermal damage as well as near-field nonthermal ablation,[29–32] the quasistatic tunneling regime ($\gamma \ll 1$) is rather impractical. In contrast, the intermediate regime ($\gamma \approx 1$) is much more attractive. However, in this regime, the nature of photoemission and the corresponding electron dynamics are still poorly understood, despite being of crucial importance for investigating the limitations on the speed and bandwidth of on-chip ultrafast electronic devices. The pioneering work in ref. [28] left several important questions open. For instance, it suggested that dynamical lowering of the barrier (Schottky effect) can significantly reduce the scaling of multiphoton photoemission with intensity. However, this assumption has no analogies in other systems in strong optical fields like atoms or molecules. Besides, typical velocities of electrons in the nanogap remain unclarified, although they are crucial to understand the bandwidth limits of the plasmonic electronic devices.

Here we employ asymmetric plasmonic nanojunctions to produce ultrafast unidirectional currents in a way similar to used in ref. [28]. In contrast to ref. [28], we operate the device at room temperature and in ambient conditions. Furthermore, we develop a modification of Y–I nonadiabatic tunneling model adapted for gold nanostructures. It allows us to clarify the origin of the photoemission currents. We investigate ultrafast dynamics of electronic wavepackets in the nanojunctions, and reconsider fundamental limitations in speed and bandwidth of such optical field-driven electronic devices.

## 2. Experimental Section

Femtosecond pulses from a Ti:sapphire oscillator with a repetition rate of $r = 100$ MHz were tightly focused onto an array of asymmetric plasmonic nanojunctions. The plasmonic nanojunctions were fabricated by focused ion beam milling of a 100 nm thick Au film on a sapphire substrate. **Figure 1**a depicts an overview scanning electron microscopy (SEM) image of the nanostructure. The laser spectrum spaned from 650 to 1000 nm with a central wavelength of 840 nm. Two broadband double-chirped mirrors and a pair of fused silica wedges were employed to control the dispersion of the pulses. The pulses were characterized by dispersion-scan method[33] and the shortest duration was retrieved to be $\simeq 7.6$ fs. The laser beam diameter on the sample ws estimated to be $\approx 7$ $\mu$m, which corresponded to a simultaneous illumination of about $N \simeq 100$ unit cells of the nanojunctions. Therefore, for the highest incident pulse energy of 1 nJ, the peak electric field of the pump laser was estimated to be $E_0 \approx 1.6$ V nm$^{-1}$. Figure 1b displays a representative unit cell of the nanojunctions, which consists of a tip-to-tip triangular Au needles with a gap of 50 nm. However, the upper tip was made much sharper than the bottom one, leading to an asymmetric distribution of the near-field enhancement, as shown in Figure 1d,e. The sharper tip exhibited much higher near-field strength. As a result, an effective negative bias arised from the upper tip to the bottom one, breaking the symmetry of electronic transport. The upper Au needle acted as an emitter electrode and the bottom one functioned as a collector. Therefore, a nonzero net photoemission current was expected to be observed when integrating over the entire pulse width.

The time-integrated photoemission current $J$ was measured by a low-noise amplifier. Meanwhile, the plasmon-enhanced third harmonic generation[34,35] was employed to optimize the laser dispersion and the spatial overlap between laser focus plane and the plasmonic nanojunctions. Figure 1c shows the measured photoemission current (blue curve) and third harmonic signal (red curve) at various thickness of the inserted silica wedges. The sensitive dependence of the current on the pulse duration confirmed that the electron emission was induced by nonthermal processes, because the thermal effects do not depend on the pulse duration for femtosecond laser.[36] At the shortest pulse duration, the integrated current read $J = 0.6$ nA, which translated to 40 electrons per pulse in average. As shown in Figure 1f, the nanodevice withstands a long-term exposure.

In **Figure 2**a a log–log dependence of the photoemission current on the incident laser electric field strength ($J - E$ curve) is shown, with an observed slope of $\approx 2$. The integrated current versus the polarization of the incident laser is also studied($J$–$\theta$ curve, cf. Figure 2b). Here $\theta$ was defined as the crossing angle between electric field direction and tip-to-tip orientation of the nanojunction. The current followed a fourth-order power of $\cos\theta$, corresponding to a $J$–$E$ curve with a coefficient $n = 2$, that is, $J \propto (E^2)^2 = I^2$, consistent with directly measured $J$–$E$ curve in Figure 2a. Considering that the electric near-field enhancement factor at a nanotip is inverse proportional to its radius of curvature,[37] as shown by the SEM in Figure 1b, the ratio of photoemission rate from the emitter with respect to the collector was estimated to be $(R/r)^4 \approx 40$. Therefore, the photoemission from

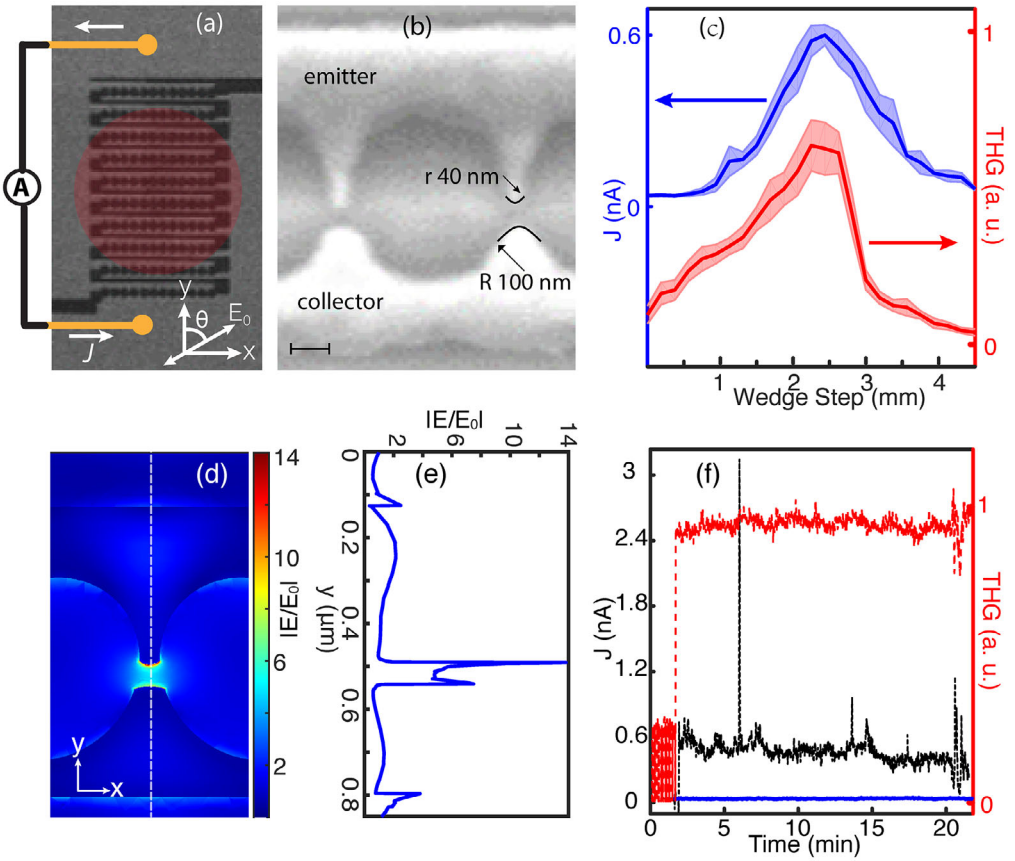


**Figure 1.** a) An overview SEM image of the plasmonic nanodevice. *J*, current; *A*, ammeter; $E_0$, optical electric field of incident laser; $\theta$, laser polarization direction with respect to y-axis. b) A high-resolution SEM image of two representative nanojunctions. c) Measured photoemission current (blue curve) and third harmonic signal (red curve) at various thickness of inserted pair of silica wedges, which controls the laser pulse duration. d) A numerical simulation of electric near-field distribution at the gold–air interface. e) Electric field enhancement factor along the dashed line in (d). f) Temporal evolution of dark current (blue curve) of the device, photoemission current (black curve), and third-harmonic generation (red curve) from the device.

the collector is ignored in the below theoretical sections. It should be pointed out that these results also agree with those of ref. [28]. However,the photoemission process was investigated using the time-domain rather than frequency-domain approach, and a conclusion opposite to that of ref. [28] was drawn, as discussed later.

## 3. Theoretical Description

### 3.1. Yudin–Ivanov Approach

For the near-field enhancement in our structure the Keldysh parameter is estimated to be in the intermediate range (c.f., gray area in the inset of Figure 2a). In the framework of atomic physics, a model named Y–I formula[6] works well in the range from multiphoton to tunneling regime (red curve in the inset of Figure 2a) and keeps correct inter-and intra-cycle ionization dynamics. Assuming the driving field in the form of $E(t) = \mathcal{E}(t)\cos\omega t$, where $\cos\omega t$ denotes the fast oscillating component, and $\mathcal{E}(t)$ the slow-varying envelope, the cycle-resolved ionization rate $\Gamma$ is given by (in atomic units, that is, frequency $\omega$, time $t$, ionization potential $\phi$, and field $\mathcal{E}$ are measured in the corresponding Hartree units $\omega_a = 0.26$ rad as$^{-1}$, $t_a = 24.2$ as, $\phi_a = 27.21$ eV, and $\mathcal{E}_a = 514.2$ V nm$^{-1}$):

$$\Gamma(t) = \frac{\pi}{\tau_T}\exp\left(-\sigma_0\frac{\mathcal{E}(t)^2}{\omega^3}\right)\left[\frac{2\kappa^3}{\mathcal{E}(t)}\right]^{2Z/\kappa}\exp\left[-\frac{\mathcal{E}(t)^2}{2\omega^3}\sigma_1\sin^2(\omega t)\right] \quad (1)$$

Here $Z$ is the effective atomic charge, $\kappa = \sqrt{2\phi}$, $\sigma_0 = \frac{1}{2}(\gamma^2 + \frac{1}{2})\ln C - \frac{1}{2}\gamma\sqrt{1+\gamma^2}$, $C = 1 + 2\gamma\sqrt{1+\gamma^2} + 2\gamma^2$, and $\sigma_1 = \ln C - 2\gamma/\sqrt{1+\gamma^2}$. The averaged photoemission rate over a single optical cycle of Equation (1) reads (in atomic units):

$$\Gamma_{av} = \frac{\pi}{\tau_T}\exp\left(-\sigma_0\frac{\mathcal{E}(t)^2}{\omega^3}\right)\left[\frac{2\kappa^3}{\mathcal{E}(t)}\right]^{2Z/\kappa}\left[\frac{2\omega^3}{\pi\mathcal{E}(t)^2\sigma_1}\right]^{1/2} \quad (2)$$

To proceed further, it is important to understand the basic idea behind the approach leading to Equation (1) and Equation (2). The population in continuum $W$ is represented as an integral over all partial amplitudes $a_p$ of the ionized electron with the

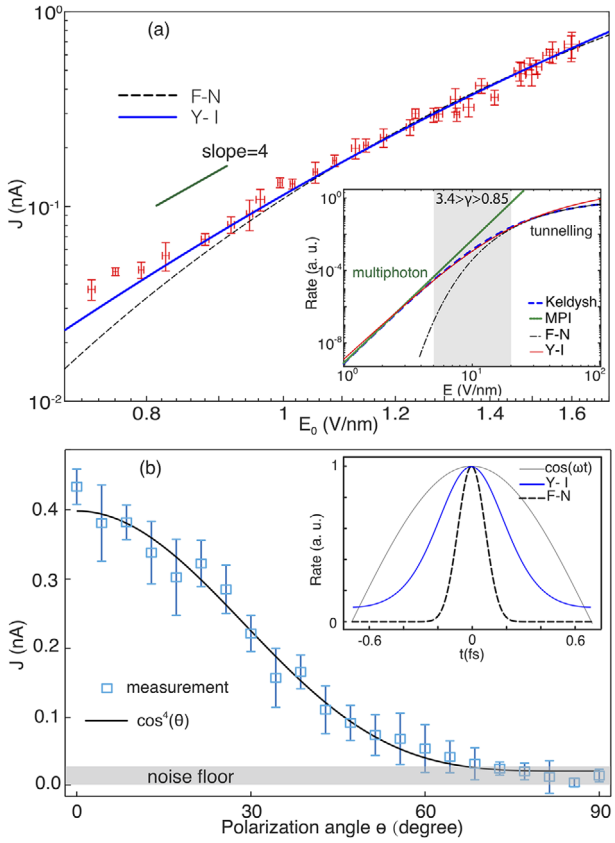


**Figure 2.** a) Experimentally measured photoemission current as a function of incident electric field strength $E_0$, F–N, Fowler–Nordheim model; Y–I, Yudin–Ivanov model. Inset: photoemission rate versus laser field strength according to the Yudin-Ivanov model (red solid curve) in comparison to multiphoton model (MPI, green solid line, rate proportional to $I^2$, where $I$ is the field intensity), F–N model (black dashed-dotted curve) and Keldysh formula (blue dashed curve).[1] b) Photoemission current $J$ (blue squares) versus the laser polarization direction $\theta$ in a good agreement with the function $J \approx \cos^4\theta$, where $\theta$ is the polarization angle (black curve). Inset: Instantaneous photoemission rate over a half cycle of laser pulse. Gray curve shows the electric field. Blue solid and black dashed curves depict nonadiabatic and quasistatic tunneling rates, respectively.

momentum $\mathbf{p}$: $W = \int_{\mathrm{p}} |a_{\mathrm{p}}|^2 d^3p$. The corresponding amplitude $a_{\mathrm{p}}$, under reasonable approximations can be obtained as

$$a_{\mathrm{p}} \approx \int_{-\infty}^{t} e^{-iS(t,t')/\hbar} \mathrm{d}t' \tag{3}$$

where $S(t, t')$ is the action:

$$S(t,t') = (\phi + \frac{p^2}{2m})(t-t') + \frac{1}{2m}\int_{t'}^{t} \left(\mathbf{p} + e\mathbf{A}(t'')\right)^2 \mathrm{d}t'' \tag{4}$$

where $\mathbf{A}(t)$ is the vector potential corresponding to the driving electric field $E(t)$. Following Equation (3), every amplitude $a_{\mathrm{p}}$ is the result of summation over all partial amplitudes, each having the phase $S(t, t')$ defined by Equation (4). The first term in Equation (4) corresponds to phase shift gained by overcoming the barrier, and the second term, so-called Volkov phase, corresponds to the phase electron gains in the electric field. Action $S(t, t')$ changes quickly for all points except the stationary ones, that is, obeying $\partial S/\partial t' = 0$. As a result, integration over the fast oscillating argument yields zero everywhere except at the stationary points (this fact constitutes the essence of so-called stationary phase, or saddle-point, method). The stationary condition results in a complex value of $t'$ equal to $t'_{\mathrm{s}}$, which can be found analytically. The ionization rate can be, up to the insignificant prefactor, calculated as $\Gamma(t) \approx \exp(-2im[S(t, t'_0)]/\hbar)$. Under reasonable approximations, this expression can be calculated analytically and gives rise to Equation (1).

The Y–I model, as mentioned above, is written for a rather general case, without the details of the potential. The only parameters referring to a particular system are the effective charge $Z$ and the ionization potential $\phi$. For gold nanostructures, we should take into account the ability of electron density on the surface to redistribute, on a femtosecond time scale, to "screen" the ionized electron. This screening is in a good approximation described by the mirror-charge model.[38,39] In this model, if we consider an ideal metal, the outgoing electron "feels" a charge at the position mirrored relative to the metal surface, but with the charge sign inverted. The distance from electron to this effective "ion," represented by mirrored charge, is twice the distance to the surface. Thus the attraction force becomes four times smaller than for the case of an electron and a single atom. This attraction force reduction can be taken into account by introducing the effective charge 1/4 instead of 1 in the Y–I model. Furthermore, in a non-ideal metal, the effective charge value is modified by a factor $|(1-\epsilon)/(1+\epsilon)|$, where $\epsilon$ is the complex susceptibility of the metal. As a result, the effective charge in Equation (1) is governed by the equation:

$$Z = \frac{1}{4}\left|\frac{1-\epsilon}{1+\epsilon}\right| \tag{5}$$

We fit the experimental data in Figure 2a by the modified Y–I model and obtain the field enhancement factor to be $g \approx 14.2$. This is a very reasonable value which is in a good agreement with the numerical simulation (c.f. Figure 1d,e). Accordingly, the Keldysh parameter $\gamma$ in our experiments is evaluated to be in the range from 0.8 to 1.7. The fitting was made without considering the spatial profile of the pulse. It is however easy to see that in the present case, taking into account the Gaussian profile leads to only a constant pre-factor 1/4. Indeed, since we have, with a good precision $J \approx E_0^4$, spatial integrating of the current $J(r)$ (were $r$ is the radial coordinate) taking into the Gaussian profile of the field $E_0 \approx \exp(-r^2/2\sigma^2)$ ($\sigma$ is the pulse width) will give the constant factor 1/4 in comparison with the same integration, performed over the constant-field distribution with the same area.

As shown in the inset of Figure 2a, the Y–I formula approaches the multiphoton limit at low intensities, and approximates the tunneling limit as given by the F–N equation at high intensities. We remark that there is another analytical expression, so-called Keldysh formula,[1,40] which works in the tunneling, multiphoton and intermediate regimes as well. It is obtained using the same stationary phase method as the Y–I formula, but the corresponding integrals are taken in the frequency space. However, the advantages of the Y–I formula are the applicability to very short (yet single-color) pulses and a possibility to describe the dynamics inside the laser cycle (c.f. the inset in Figure 2b), whereas

the Keldysh equation was written for the quasi-monochromatic wave and gives only cycle-averaged ionization rate. On the other hand, we note the recent works[41,42] where the Keldysh formula was extended to ultrashort pulses of some particular shapes. For the particular parameters presented here there is no possibility to reliably differentiate between Y–I and Keldysh formulas. This differentiation can be done, for instance, for even shorter pulses in the case if the CEP control is implemented. In this situation the change of the CEP leads to change of the result in the case of Y–I formula but in the framework of the Keldysh formula the result should be CEP-independent.

As depicted in Figure 2, the current $J$ is nearly proportional to $I^2$. According to the Y–I model, we identify this $I^2$-law as an indication that we are in the intermediate regime, and thus invoking the Schottky effect is not necessary to explain this behavior as it is done in refs. [28, 40]. In the following paragraphs, we return to this point in details.

### 3.2. Schrödinger Equation

To get deeper insight into the dynamics of the photoemission and subsequent electron propagation between the tips, we simulate the emission by numerical solution of the following 1D time-dependent Schrödinger equation (TDSE) in the Coulomb gauge ($\partial_x A = 0$):

$$i\hbar \frac{\partial \psi(x,t)}{\partial t} = \frac{1}{2m}\left[(p + eA(x,t))^2 + V(x)\right]\psi(x,t) \tag{6}$$

where $\psi(x,t)$ is the electronic wavefunction, $p = -i\hbar\frac{\partial}{\partial x}$, $A(x,t)$ is the vector potential which takes into account spatial field inhomogeneity as a pre-factor $e^{-\tilde{\alpha}x}$, $\tilde{\alpha} = 1.0\ \mathrm{ns}^{-1}$, $V(x)$ is a rectangular asymmetric potential

$$V(x) = \begin{cases} -V_0, & \text{if } |x| < a; \\ 0, & \text{if } x > a; \\ \infty, & \text{if } x < -a, \end{cases} \tag{7}$$

where $a = 0.106$ nm, $V_0 = 16.94$ eV are selected in such a way that i) the potential has exactly one bound state and ii) the ionization potential of this bound state equals to the work function of gold (5.1 eV). We note that this potential assumes that the wavefunction inside the metal is localized. It was shown that this assumption does not significantly influence the ionization rate.[9] Moreover, the experimentally observed electron spectra[8,10] and even electron dynamics[43] are good described by this rather simple approach. Therefore, it is widely used to model the ionization.[8,10–12,21,44–46] In the potential defined by Equation (7), ionization can occur only in the positive direction of $x$. The electrons leaving the emitter are accelerated by the field and propagate toward the collector. These electrons are considered to be fully absorbed, that is, reflection on the potential of the collector is neglected. We model this by adding to the potential the soft absorbing boundary $V(x) \to V(x) - i\alpha(x)$ with $\alpha = \alpha_0(1 + \mathrm{erf}((x-s)/\delta))/2$, where $\delta = 2.65$ pm, $\alpha_0 = 1$ au, and $s = 50$ nm is the distance between the emitter and collector. The simulation was made by a split-step method, with separate evaluation of the terms $\approx p^2$, $pA + Ap$, $A^2$, and $V$; the action of $p$ was calculated using the fast Fourier transform.

The resulting dynamics of the electronic wavefunction $\psi(x,t)$ is shown in **Figure 3**a for the peak driving field amplitude $gE_0 = 12.3\ \mathrm{V\ nm}^{-1}$ (corresponding to $\gamma = 1.68$, clearly in the transient regime) and pulse duration of 7 fs, according to the experiment. One can see from Figure 3a, that at every positive-field subcycle of the driving electric field, an ionization event takes place: noticeable part of the electron is released close to extremum of the electric field. As one can see from Figure 3c, the free electron density increases starting from the maximum of the electric field, achieves its maximum one quarter of the cycle later, and then decreases because some part of electrons returns back. After being ionized, the part of electron, which does not return, propagate toward the collector. Interestingly, upon the propagation the electron wavepacket is separated into distinct well-visible "beams" marked by $n = 1, 2, \ldots$, every of them propagating with velocity clearly different from the others. The field inhomogeneity plays only relatively minor role in this dynamics. If it is removed ($\tilde{\alpha} = 0$, see dashed line in Figure 3b) the beam structure remains the same, only most of the electrons move faster to the collector.

Ionized electrons reach, after some propagation, the collector, producing the current $J(t)$ given as

$$J(t) = \frac{\hbar}{2im}\left(\psi^*\frac{\partial \psi}{\partial x} - \psi\frac{\partial \psi^*}{\partial x}\right) \tag{8}$$

Here, $\psi$ is taken at the surface of the collector. The above mentioned "beams," which are visible in Figure 3a, manifest themselves as short spikes of $J(t)$ as can be seen in Figure 3b.

The nature of this dynamics becomes apparent if we consider the picture in the energy space, see Figure 3c, where the energy spectrum of the electrons in dependence on time is shown, as well as in Figure 3d, where energy spectra at specific times $t_i$, $i = 0 \ldots 3$ are presented. One can see (cf. for instance $t_0, t_1$) that in the beginning of the pulse there is no visible structure in the energy distribution of electrons. Electrons are born with a broad energy spectrum of more than 10 eV width. The energy structure sets up gradually during the next few cycles (see the time events $t_2, t_3$), and, finally close to the end of the pulse (the time event $t_3$) it settles to be peaked around the multiples of the photon energy $n\hbar\omega$. This very clearly shows that multiphoton effects (absorption of $n$ photons) appears only on the inter-cycle scale, as an interference between newly-born parts of the electron wavepacket and the parts which are already present in the continuum.

In even more clear form this inter-cycle interference is schematically shown in **Figure 4**, which illustrates the physics behind the results in Figure 3c. As it is presented in Figure 4, the newborn electrons have a broad spectrum (black-white gradient) and different phases (color gradient—in the figure we deliberately set the time origin so that the first phase is constant in energy). The interference between parts of the electronic wavepacket created at different cycles leads to clearly visible channels $n = 0, n = 1, \ldots$ after the end of the pulse. Note that in Figure 3c these dynamics start to set up already in the middle of the pulse since, unless the wavepacket is not the first one ($t_0$ in Figure 3c), the newborn parts of the wavepacket start to interfere with the previously born ones ($t_1, t_2$ in Figure 3c).

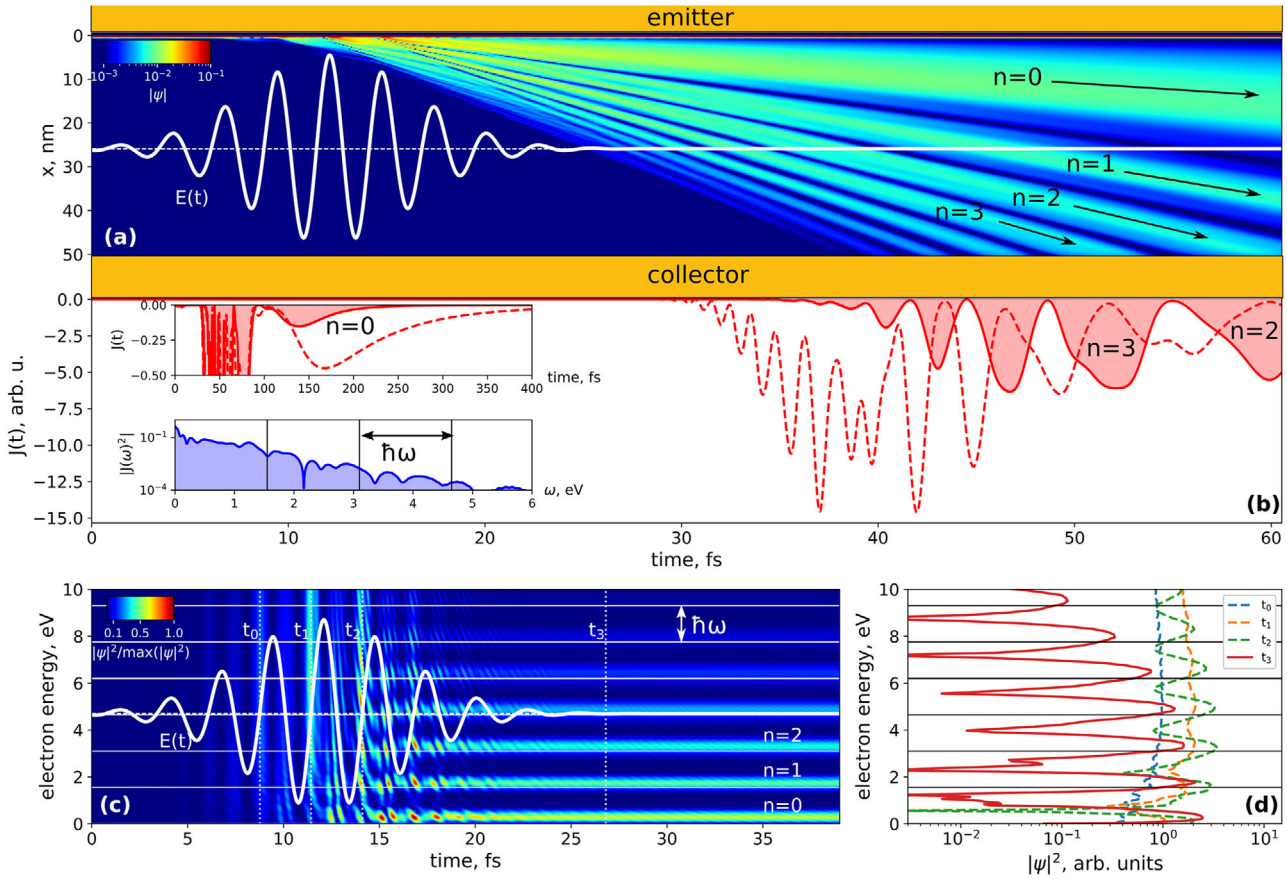


**Figure 3.** Dynamics of ionization at the emitter, and current at the collector, according to numerical simulations of the single-electron problem Equation (6) for $gE_0 = 12.3$ V nm$^{-1}$ and 7 fs pulse duration. a) The modulus of the wavefunction of the ionized electron $|\psi(x, t)|$ in dependence on $x$ and $t$. White line shows the driving electric field; as the electronic wavepacket arises in continuum and propagates, it is separated into the well-visible electronic "beams" labeled by $n = 0, 1, \ldots$. Each beam [see also (c)] corresponds to an electron absorbed approximately $n$ photons from the driving field and thus having energy $\approx n\hbar\omega$. b) The electron current $J(t)$ created on the collector surface in dependence on time $t$. Dashed red line shows the current created by a homogeneous field ($\tilde{\alpha} = 0$). The upper inset shows $J(t)$ on a larger times scale, and the lower inset depicts the spectrum of $J(t)$. The vertical lines show the energies corresponding to $n\hbar\omega$. c) Temporal evolution of the free electron energy. The white curve shows again the driving electric field, whereas the horizontal white lines show the energies corresponding to $n\hbar\omega$. d) Energy spectra at the (somewhat arbitrarily selected) times $t_i$ [marked in (c)]. In (c) and (d) one clearly sees multiphoton peaks $n = 1, 2, \ldots$ as they arise on the inter-cycle time scale due to interference, and become more and more pronounced toward the end of the pulse.

The condition of constructive interference can be easily obtained as follows: the phase shift $\Phi$ of the electron in the continuum (in the presence of the field) over the optical period $T$ is $\Phi = T(p^2/2m + U_p)/\hbar$, where $U_p = e^2\mathcal{E}^2/4m\omega^2$ is the ponderomotive energy. At the same time, the electrons in the metal (near the Fermi energy) will experience the relative phase shift $\Phi_F = -T\phi/\hbar$. Thus, the relative phase of two partial wavepackets born in the continuum at the two time instants separated by $T$ is $\Phi + \Phi_F$. The corresponding constructive interference condition $\Phi + \Phi_F = 2\pi n$ gives: $p^2/2m + U_p + I_p = n\hbar\omega$, that is, the subsequent peaks in electron energy $p^2/2m$ are separated by the photon energy $\hbar\omega$. This demonstrates that the multiphoton peaks corresponding to the absorption of $n$ photons appear from the interference between the electronic wavepackets created by different optical cycles. Inside the cycle, no such multiphoton effects can be identified. One can explain this also in the terms of the Heisenberg uncertainty relation $\Delta p_x \Delta x \geq \hbar/2$: in every ionization event, the electrons are born in the very small region surrounding the surface, of the order of $\Delta x \approx 0.1$ nm, which means uncertainty in momentum $\Delta p_x$, corresponding to the kinetic energy in the range from zero to several eV. This uncertainty in momentum is partially "regularized" on the longer, intercycle scale as described above, giving rise to the multiphoton energy structure.

From Figure 4 one can clearly see how to distinguish the impacts from different ionization channels (accomplished by absorption of different number of photons), and to estimate their relative importance: if a certain channel is present in the ionization process, there must be a corresponding peak in the electron energy distribution after the end of this pulse. The "intensity" of every particular peak allows to estimate the relative impact of different channels. To distinguish different channels is important in view of refs. [28, 40] where so called Schottky effect is proposed to describe the current-versus-intensity behavior. The Schottky-effect-based explanation suggests that the potential barrier is lowered by the external field (see Figure 4, red dashed line) so that two instead of four photons are sufficient for ionization.

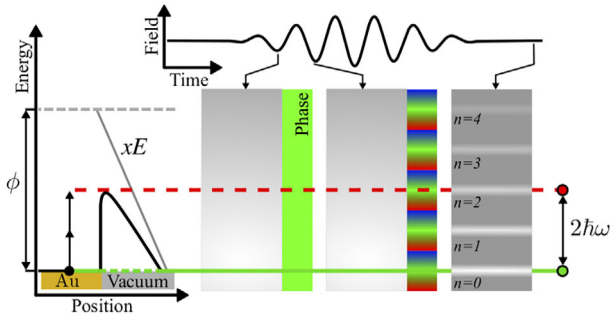


**Figure 4.** Schematic representation of different photon absorption channels by electron ionization. This picture is to be compared to Figure 3c. At every ionization event the electrons are born with a broad unstructured energy spectrum (rectangles with black-white gradient), and phase Φ (colored gradients) which depends on the temporal position of the ionization event ($\Phi \approx t - t_0$, here $t_0$ is set so that $t - t_0 = 0$ at the first of two depicted events). The interference of these wavepackets leads to visible periodic modulations of the energy distribution after the pulse, which can be interpreted as multiphoton channels $n = 0, n = 1, \ldots$. Thus, after the end of the pulse one can distinguish between the channels, for instance direct ionization channel (green horizontal line) and ionization via Schottky effect (red dashed line). The amplitudes of the channels allow to estimate the relative importance of each channel.

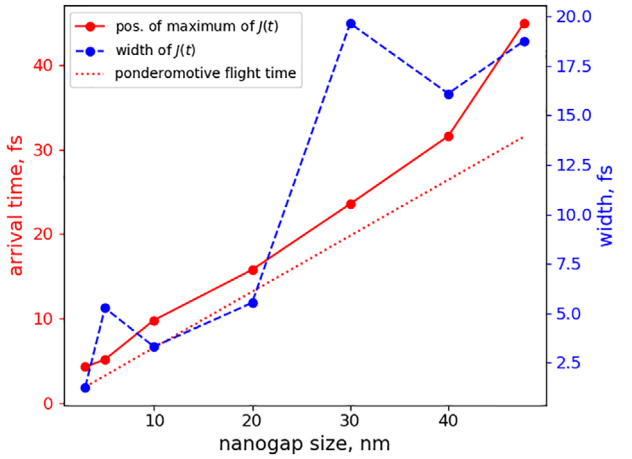


**Figure 5.** The position of the maximum of the current $J(t)$ at the collector (red points and red solid line) relative to the pump pulse center (thus denoting the arriving time of the electron at the collector), as well as the width of $J(t)$ (blue points and blue dashed line), as a function of the size of the nanogap, obtained by simulations of Equation (6). Red dotted line shows the arrival time of an electron at the collector, if the electron's energy is equal to $U_p$, the ponderomotive energy.

This channel corresponds to $n = 2$ in Figure 4 and in Figure 3, in contrast to "direct" tunneling which corresponds to $n = 0$ (green line in Figure 4).

As one can see from Figures 3c and 4, the peak at $2\hbar\omega$ ($n = 2$) which could correspond to Schottky effect indeed appears, but it is also clearly not a dominating one. The peak corresponding to "direct" tunneling $n = 0$ has even higher amplitude. The "anomalous" dependence of the current $J$ on intensity $I$ ($J \approx I^2$) is thus not explained by the Schottky effect but by the fact that we are in the transition region from tunnel to multiphoton ionization, and the impacts from different channels $n$ have close amplitudes and add up to give the observed scaling.

Interestingly, the emergence of the multiphoton energy structure of the electronic wavepacket allows to understand, what happens with an electron as it propagates between the tips (Figure 3a) and thus to interpret the resulting current $J(t)$ in Figure 3b. Indeed, different electronic "beams" in Figure 3a and different peaks in $J(t)$ in Figure 3b correspond to different peaks in the electron energy in Figure 3c. The slowest beam $n = 0$ corresponds to the lowest-energy electrons, which absorbed just enough energy to get through the barrier; $n = 1$ corresponds to the electrons which absorbed one photon more, and so on. Every beam corresponds to electrons which have a mean velocity around $v = \sqrt{2n\hbar\omega/m}$. Because of diffractive spreading of the wavepacket, its width grows as $\sqrt{t}$. The slowest wavepackets spend longer time to overcome the nanogap, and thus spread stronger. The resulting structure of the current $J(t)$ in Figure 3b is thus the collection of peaks, every of them having increasing width due to increasing diffractive spreading. Although the peak with $n = 0$ carriers the largest part of the whole electron probability, it is also broadened at strongest, so that as it arrives to the collector, it has a relatively small amplitude (see inset to Figure 3b where this peak is visualized). The same is true for other, not too high values of $n$: the diffractive spreading significantly decreases the corresponding amplitude in $J(t)$. On the other hand, the amount of the electrons contained in the subsequent $n$ decreases as $n$ increases. The global maximum of $J(t)$ is thus the result of this interplay between the diffractive spreading and energy balance of individual beams. In our configuration, the most intense peaks appear at around $n = 7$–$11$.

As follows from Figure 3b, although the shape of the current bunch occurring at the collector is rather complicated, one can define some quantities characterizing it, in particular i) the time delay in respect to the center of the pump pulse, and ii) the duration of the bunch. Here we define the above mentioned delay via the position (in time) of the highest peak of $J(t)$, and the width is defined by full-width half-maximum. Such defined delay and duration are shown in Figure 4 for different sizes $s$ of the nanogap. For the particular case of Figure 3b with $s = 50$ nm, the current $J(t)$ peaks at around 40 fs (that is, delayed by around 30 fs from the pulse center) and the duration of the current bunch is of the order of 15 fs.

One can see from **Figure 5** that the delay of the current spike does not, generally speaking, grow linearly with the gap size. This is explained by the reshaping of the electronic wavepacket described above. This reshaping is, as already mentioned, a result of interplay between the diffractive spreading and electron energy balance. Nevertheless, if we compare the delay of $J(t)$ with the naïve estimation for the flight time $t_f = s/v_p$, where $s$ is the size of the nanogap, and $v_p = \sqrt{2U_p/m}$ is the mean velocity corresponding to the ponderomotive energy $U_p = e^2\mathcal{E}^2/4m\omega^2$ (red dotted line in Figure 4), we observe quite a good correspondence. This indicates that, although the electron wavepacket has a complicated shape, its propagation can be described with a velocity which corresponds to the mean ponderomotive energy of the electron in the field. The speed of the devices increases thus with decrease of the nanogap. Recently, the gaps in the order of nm were achieved.[47]

## 4. Conclusion

In conclusion, we utilized an array of spatially asymmetric nanojunctions to break the symmetry of the ionization process and to generate an ultrafast optically switchable on-chip electronic current at room temperature and under the standard conditions. Generation of currents up to 0.6 nA by a few-cycle driver pulse with a random carrier-envelope phase, without using a DC bias, is possible in this way. Introducing CEP control to this scheme could additionally increase the efficiency, but for relatively long pulse durations we used here such increase should be only minor. We have extended the Y–I model, which works well for the tunneling, multiphoton and intermediate regimes of atoms, to gold nanostructures. The excellent agreement of the Y–I model allowed to establish the leading current formation mechanism: the observed data can be well explained by assuming nonadiabatic tunneling through the barrier. This conclusion is supported by direct simulations of electron ionization dynamics using the time-dependent Schrödinger equation, which demonstrated, that any effects manifesting as an absorption of several photons occur by the inter-cycle interference of electronic wavepackets, and are undefined on the sub-cycle time scale. No signatures of prevailing influence of the Schottky barrier lowering was found. In contrast, the unusual current scaling $J \approx I^2$ is explained via the joint influence of all multiphoton channels taking place in the nonaddiabatic tunneling regime, that is, in the transition region between tunneling and multiphoton ionization. Our detailed view of the electron dynamics allowed to determine the limits on the speed of such devices. We observe that the shape of the electron wavepacket is rather complicated: the flying electrons are separated into "beams," each of them having the velocity corresponding to certain number of absorbed photons. Nevertheless, in average, the flight time of electrons in the nanogap is determined, to a good precision, by the ponderomotive velocity of electrons in the driving field. This suggests that the primary way to increase the speed could be not only to decrease the gap but also to increase the ponderomotive energy, which does not automatically mean increasing the peak field: multicolor driving fields could also help at this.[48]

## Acknowledgements

L.S. and I.B. contributed equally to this work. The authors acknowledge support from Deutsche Forschungsgemeinschaft (DFG) (KO 3798/4-1, BA 4156/4-2, MO 850-19/2, MO 850-23/1) and from German Research Foundation under Germany's Excellence Strategy EXC-2123 and Germany's Excellence Strategy within the Cluster of Excellence PhoenixD (EXC 2122, Project ID 390833453), Lower Saxony through 'Quanten und Nanometrologie' (QUANOMET, Project Nanophotonik). H.G. and B.F. acknowledge funding by ERC (ComplexPlas and 3D Printedoptics) and DFG (SPP1839). A.H. acknowledges funding from MSCA RISE project ID 823897. C.L. gratefully fully acknowledges the DFG (SPP 1839 and SPP1840) for financial support. L.S. is supported by National Natural Science Foundation of China (No. 12004314), the open project program of Wuhan National Laboratory for Optoelectronics No. 2020WNLOKF004 and Zhejiang Provincial Natural Science Foundation of China under Grant No. Q21A040010. MI acknowledges support by the DFG priority program QUTIF under grant agreement IV 152/6-2 and the funding from the European Union's Horizon 2020 research and innovation programme under grant agreement No 899794.

Open access funding enabled and organized by Projekt DEAL.

## Conflict of Interest

The authors declare no conflict of interest.

## Data Availability Statement

Research data are not shared.

## Keywords

ionization, nanostructures, optoelectronics

Received: October 28, 2020
Revised: April 9, 2021
Published online: June 16, 2021

[1] L. Keldysh, *Sov. Phys. J. Exp. Theor. Phys.* **1965**, *20*, 1307.
[2] E. Mevel, P. Breger, R. Trainham, G. Petite, P. Agostini, A. Migus, J.-P. Chambaret, A. Antonetti, *Phys. Rev. Lett.* **1993**, *70*, 406.
[3] F. Lindner, M. G. Schätzel, H. Walther, A. Baltuška, E. Goulielmakis, F. Krausz, D. Milošević, D. Bauer, W. Becker, G. G. Paulus, *Phys. Rev. Lett.* **2005**, *95*, 040401.
[4] I. Babushkin, C. Brée, C. M. Dietrich, A. Demircan, U. Morgner, A. Husakou, *J. Mod. Opt.* **2017**, *64*, 1078.
[5] H. Zimmermann, S. Patchkovskii, M. Ivanov, U. Eichmann, *Phys. Rev. Lett.* **2017**, *118*, 013003.
[6] G. L. Yudin, M. Y. Ivanov, *Phys. Rev. A* **2001**, *64*, 013409.
[7] R. Bormann, M. Gulde, A. Weismann, S. Yalunin, C. Ropers, *Phys. Rev. Lett.* **2010**, *105*, 147601.
[8] M. Krüger, M. Schenk, P. Hommelhoff, *Nature* **2011**, *475*, 78.
[9] S. V. Yalunin, M. Gulde, C. Ropers, *Phys. Rev. B* **2011**, *84*, 195426.
[10] M. Krüger, M. Schenk, M. Förster, P. Hommelhoff, *J. Phys. B: At., Mol. Opt. Phys.* **2012**, *45*, 074006.
[11] M. Krüger, M. Schenk, P. Hommelhoff, G. Wachter, L. Lemell, J. Burgdörfer, *New J. Phys.* **2012**, *14*, 8085019.
[12] M. Krüger, C. Lemell, G. Wachter, J. Burgdörfer, P. Hommelhoff, *J. Phys. B: At., Mol. Opt. Phys.* **2018**, *51*, 172001.
[13] P. Dombi, A. Hörl, P. Rácz, I. Máron, A. Tügler, J. R. Krenn, U. Hohenester, *Nano Lett.* **2013**, *13*, 674.
[14] G. Herink, D. Solli, M. Gulde, C. Ropers, *Nature* **2012**, *483*, 190.
[15] B. Piglosiewicz, S. Schmidt, D. J. Park, J. Vogelsang, P. Groß, C. Manzoni, P. Farinello, G. Cerullo, C. Lienau, *Nat. Photonics* **2014**, *8*, 37.
[16] P. Racz, Z. Papa, I. Márton, J. Budai, P. Wróbel, T. Stefaniuk, C. Prietl, J. R. Krenn, P. Dombi, *Nano Lett.* **2017**, *17*, 1181.
[17] D. J. Park, B. Piglosiewicz, S. Schmidt, H. Kollmann, M. Mascheck, C. Lienau, *Phys. Rev. Lett.* **2012**, *109*, 244803.
[18] J. Vogelsang, J. Robin, B. J. Nagy, P. Dombi, D. Rosenkranz, M. Schiek, P. Groß, C. Lienau, *Nano Lett.* **2015**, *15*, 4685.
[19] F. Schertz, M. Schmelzeisen, M. Kreiter, H.-J. Elmers, G. Schönhense, *Phys. Rev. Lett.* **2012**, *108*, 237602.
[20] J. Robin, J. Vogelsang, B. J. Nagy, P. Dombi, P. Groß, C. Lienau, in *Conf. on Lasers and Electro-Optics*, OSA Publishing, Washington, DC **2016**, p. FTh4B.
[21] P. Dombi, Z. Pápa, J. Vogelsang, S. V. Yalunin, M. Sivis, G. Herink, S. Schäfer, P. Groß, C. Ropers, C. Lienau, *Rev. Mod. Phys.* **2020**, *92*, 025003.
[22] K. E. Priebe, C. Rathje, S. V. Yalunin, T. Hohage, A. Feist, S. Schäfer, C. Ropers, *Nat. Photonics* **2017**, *11*, 793.
[23] A. Feist, N. Bach, N. R. da Silva, T. Danz, M. Möller, K. E. Priebe, T. Domröse, J. G. Gatzmann, S. Rost, J. Schauss, S. Strauch, R. Bormann, M. Sivis, S. Schäfer, C. Ropers, *Ultramicroscopy* **2017**, *176*, 63.

[24] S. Zhou, K. Chen, M. T. Cole, Z. Li, J. Chen, C. Li, Q. Dai, *Adv. Mater.* **2019**, 1805845.
[25] J. Schoetz, Z. Wang, E. Pisanty, M. Lewenstein, M. F. Kling, M. Ciappina, *ACS Photonics* **2019**, *6*, 3057.
[26] T. Rybka, M. Ludwig, M. F. Schmalz, V. Knittel, D. Brida, A. Leitenstorfer, *Nat. Photonics* **2016**, *10*, 667.
[27] M. Ludwig, G. Aguirregabiria, F. Ritzkowsky, T. Rybka, D. C. Marinica, J. Aizpurua, A. G. Borisov, A. Leitenstorfer, D. Brida, *Nat. Phys.* **2019**, *16*, 341.
[28] C. Karnetzky, P. Zimmermann, C. Trummer, C. D. Sierra, M. Wörle, R. Kienberger, A. Holleitner, *Nat. Commun.* **2018**, *9*, 2471.
[29] N. Pfullmann, C. Waltermann, M. Noack, S. Rausch, T. Nagy, C. Reinhardt, M. Kovačev, V. Knittel, R. Bratschitsch, D. Akemeier, A. Hutten, A. Leitenstorfer, U. Morgner, *New J. Phys.* **2013**, *15*, 093027.
[30] W. P. Putnam, R. G. Hobbs, P. D. Keathley, K. K. Berggren, F. X. Kärtner, *Nat. Phys.* **2017**, *13*, 335.
[31] L. Shi, B. Iwan, Q. Ripault, J. R. Andrade, S. Han, H. Kim, W. Boutu, D. Franz, R. Nicolas, T. Heidenblut, C. Reinhardt, B. Bastiaens, T. Nagy, I. Babushkin, U. Morgner, S.-W. Kim, G. Steinmeyer, H. Merdji, M. Kovčev, *Phys. Rev. Appl.* **2018**, *9*, 024001.
[32] L. Shi, R. Nicolas, J. R. Andrade, W. Boutu, D. Franz, T. Heidenblut, C. Reinhardt, U. Morgner, H. Merdji, M. Kovacev, *ACS Photonics* **2018**, *5*, 1208.
[33] L. Shi, J. R. Andrade, A. Tajalli, J. Geng, J.-M. Yi, T. Heidenblut, F. Segerink, I. Babushkin, M. Kholodtsova, H. Merdji, B. Bastiaens, U. Morgner, Milutin Kovacev, *Nano Lett.* **2019**, *19*, 4779.
[34] M. Hentschel, T. Utikal, H. Giessen, M. Lippitz, *Nano Lett.* **2012**, *12*, 3778.
[35] L. Shi, B. Iwan, R. Nicolas, Q. Ripault, J. R. Andrade, S. Han, H. Kim, W. Boutu, D. Franz, T. Heidenblut, C. Reinhardt, H. M. J. Bastiaens, G. T. Nagy, I. Babushkin, U. Morgner, S.-W. Kim, G. Steinmeyer, H. Merdji, M. Kovacev, *Optica* **2017**, *4*, 1038.
[36] A. Plech, V. Kotaidis, M. Lorenc, J. Boneberg, *Nat. Phys.* **2006**, *2*, 44.
[37] L. Novotny, B. Hecht, *Principles of Nano-Optics*, Cambridge University Press, Cambridge **2012**.
[38] J. D. Jackson, *Classical Electrodynamics*, Wiley, New York **1962**.
[39] V. Sahni, K.-P. Bohnen, *Phys. Rev. B* **1985**, *31*, 7651.
[40] P. Zimmermann, A. Hötger, N. Fernandez, A. Nolinder, K. Müller, J. J. Finley, A. W. Holleitner, *Nano Lett.* **2019**, *19*, 1172.
[41] L. V. Keldysh, *Phys.-Usp.* **2017**, *60*, 1187.
[42] S. Kim, T. Schmude, G. Burkard, A. S. Moskalenko, *arXiv:2011.15125* **2020**.
[43] Ph. Dienstbier, personal communication, **2021**.
[44] P. Hommelhoff, C. Kealhofer, M. A. Kasevich, in *IEEE International Frequency Control Symp. and Exposition*, IEEE, Piscataway, NJ **2006**, pp. 470–474.
[45] S. V. Yalunin, G. Herink, D. R. Solli, M. Krüger, P. Hommelhoff, M. Diehn, A. Munk, C. Ropers, *Ann. Phys.* **2013**, *525*, L12.
[46] P. D. Keathley, A. Sell, W. P. Putnam, S. Guerrera, L. Velásquez-García, F. X. Kärtner, *Ann. Phys.* **2013**, *525*, 144.
[47] M. Garg, K. Kern, *Science* **2020**, *367*, 411.
[48] P. G. d. A. Martínez, I. Babushkin, L. Bergé, S. Skupin, E. Cabrera-Granado, C. Köhler, U. Morgner, A. Husakou, J. Herrmann, *Phys. Rev. Lett.* **2015**, *114*, 183901.